IEEE Access
Multidisciplinary | Rapid Review | Open Access Journal

Received December 7, 2018, accepted February 4, 2019, date of publication February 15, 2019, date of current version March 5, 2019.

Digital Object Identifier 10.1109/ACCESS.2019.2899674

Ground Surface Filtering of 3D Point Clouds Based on Hybrid Regression Technique

KAIQI LIU[1], WENGUANG WANG[1], RATNASINGHAM THARMARASA[2], JUN WANG[1], AND YAN ZUO[3]

[1]School of Electronic and Information Engineering, Beihang University, Beijing 100191, China
[2]Department of Electrical and Computer Engineering, McMaster University, Hamilton, ON L8S 4K1, Canada
[3]School of Automation, Hangzhou Dianzi University, Hangzhou 310018, China

Corresponding author: Wenguang Wang (wwenguang@buaa.edu.cn)

This work was supported in part by the National Natural Science Foundation of China under Grant 61771028, Grant 61671035, and Grant 61673146.

ABSTRACT Lidar has received a lot of attention due to its precise ranging accuracy. Ground points filtering is an important task in point clouds processing. It's a challenge to model the ground surface and filter the point clouds accurately in the case of complex ground undulations, occlusions, and sparse point clouds. A novel ground surface modeling method based on a hybrid regression technique is proposed in this paper. The method integrates Gaussian process regression (GPR) and robust locally weighted regression (RLWR) by dividing the point clouds that are projected on the polar grid map into radial and circumferential filtering processes to form a hybrid regression model, which has the ability to eliminate the influence of outliers and model the ground surface robustly. First, the RLWR combined with gradient filter is applied to fit the sampled points in the radial direction, which will exclude outliers and get the fitting ground line. All radial fitting lines constitute the seed skeleton of the whole plane. Then, based on the seeds in the same circumferential of the skeleton, the GPR is applied to construct the ground surface model. The comparative experiments are implemented quantitatively and qualitatively on the simulated point clouds and measured data. The results show that the proposed method performs well in most real scenarios, even in the cases of ground undulation, occlusion, and sparse point clouds.

INDEX TERMS Lidar, point clouds, ground filtering, Gaussian process regression (GPR), robust locally weighted regression (RLWR).

I. INTRODUCTION

In the field of mobile mapping, Lidar becomes a standard sensor with high accuracy [1]. Lidar can construct the 3D environment with point clouds for environment perception, which is of significance for complex industrial architectures representation [2], autonomous driving development [3], [4], and intelligent transportation construction [5].

Classifying the point clouds into ground and non-ground is an important task in point clouds processing. Filtering out the ground points can effectively reduce the computational complexity of aboveground objects classification, feature extraction, and objects detection [6], [7]. The same argument is valid when the objective is to extract the curbs and footpath with the filtered ground points [8]. To divide the point clouds into ground and non-ground, many filtering methods have been proposed. According to [8] and [9], the filtering methods can be classified as morphology-based filtering [10], [11], elevation maps filtering [12], [13], model-based filtering [5], [14], etc. The theories of the first two methods are intuitive and the methods are easy to implement. In [15], a scan-line-based filtering algorithm is proposed. The error rate of the ground extraction is 0.674%. In [16], a histogram-based method is utilized for ground removal to reduce the volume of data. The model-based method is an effective way to construct the complex ground surface model, in which Markov Random Field (MRF) and Gaussian Process Regression (GPR) are commonly used.

In [5], a MRF model with a belief propagation (BP) algorithm is applied for road extraction. A robust road detection method is proposed in [17] with the inference algorithm based on MRF and Loopy Belief Propagation (LBP). Motivated by [5] and [17], a cost-based ground measurement model

The associate editor coordinating the review of this manuscript and approving it for publication was Siddhartha Bhattacharyya.

incorporated into a MRF and a LBP is proposed to filter the ground [9]. The true positive rate of the classification can be higher than 92% in both simple rough terrain and complex off-road environment. Conditional Random Field (CRF) is a variant of MRF. In [18], a machine learning approach to automatically extract digital terrain models is proposed. The overall error rate of the method is 3.46% in the case of ignoring scattering and multiple returns.

Another popular model-based filtering method is based on GPR. In [14], Gaussian Process Incremental Sample Consensus (GP-INSAC) and Mesh Based Segmentation are proposed for filtering the point clouds received from the Velodyne scanner. After evaluating these methods on several sets of hand labeled data, the match percentages of the two methods are 89% and 92%, respectively. In [19], a fast ground filtering method with a 2D polar grid map is proposed. Compared with RBNN algorithm and 2.5D projection method, the method has the advantage in computation. Based on [14] and [19], a GP-Based method is proposed [3] and gets a trade-off between the high filtering accuracy of [14] and high operating rate of [19].

Motivated by the method in [3], a hybrid regression method is proposed to model the ground surface and filter the ground points. The robust locally weighted regression (RLWR) techniques [8], which can eliminate the influence of outliers in fitting, are applied for building the seed skeleton with sampled point clouds from polar grid map. Then, the seed skeleton is divided into concentric rings to predict the elevation model of the ground surface with GPR. After obtaining the ground surface elevation model, a predefined height threshold is used for filtering the ground points. The major advantages of the proposed method are two-fold. First, the hybrid regression process can eliminate the influence of outliers on the modeling and avoid specifying local parameters when predicting the surface model with sparse point clouds. The second advantage is about the application of the continuity of whole plane with 1D fitting in two orthogonal directions instead of 2D processing. With the continuity of two directions, the method can model the ground surface accurately.

The main objective of this study is to demonstrate a novel ground surface modeling method for 3D point clouds filtering. The basic knowledge of GPR and RLWR is described in section II. The proposed ground surface modeling method is detailed in section III. The comparative experiments and discussions are shown in section IV. Concluding remarks are given in section V.

II. PRELIMINARIES

In this section, the basic knowledge of polar grid map, GPR, and RLWR are introduced, respectively. In the field of intelligent vehicles, the superiority of building the polar grid map is that it can adapt to the distribution of point clouds and effectively reduce the dimension of data. RLWR and GPR are two kinds of regression techniques that can be applied to model the ground surface [8], [20].

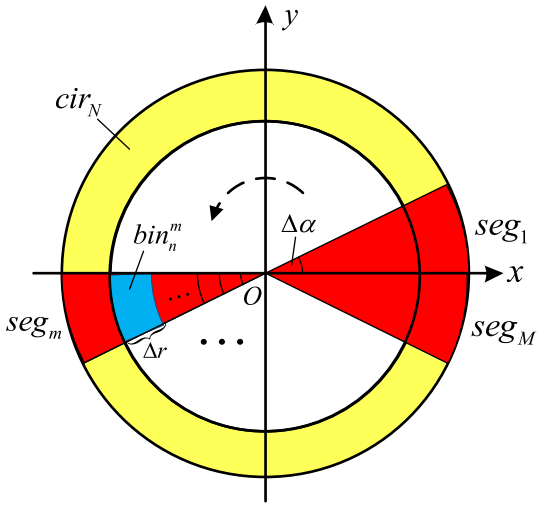

FIGURE 1. The projection process of point clouds on polar grid map. The red sectors represent *segments*, the yellow ring denotes *circle*. The overlap of a *segment* and a *circle* is called a *bin*. $\Delta\alpha$ is the angle of *segments*. Δr is the radial length.

A. POINT CLOUDS REPRESENTATION

Considering the physical characteristics of the vehicle-mounted Lidar, for example HDL-64E, the polar grid map is utilized to represent the received point clouds $P = \{p_1, p_2, \ldots, p_{N_P}\}$, where N_P represents the number of points in a frame of point clouds. $p_i = (x_i, y_i, z_i)$, $i = 1, 2, \ldots, N_P$ is the Euclidean coordinate of the point. The point clouds data are projected onto a horizontal plane and are denoted by polar coordinates. The point clouds can be divided into M sectors as well as N circular segmentations. The sectors have the same central angle, and the circular segmentations are a series of concentric rings. In this paper, the sector and the circular segmentation are called *segment* and *circle*, respectively. The overlap of a *segment* and a *circle* is represented by a *bin*. The division process is shown in Fig. 1.

The position of point p_i can be expressed by *segment* and *circle* as follows.

$$seg(p_i) = \left\lceil \frac{\text{atan2}(x_i, y_i)}{\Delta\alpha} \right\rceil \tag{1}$$

$$cir(p_i) = \left\lceil \frac{\sqrt{x_i^2 + y_i^2}}{\Delta r} \right\rceil \tag{2}$$

where $\lceil\cdot\rceil$ denotes the ceil operation, atan2$(\cdot)$ is utilized to compute the angle between the vector $\vec{v} = (x_i, y_i)$ and the positive x-axis, whose range is $[0, 2\pi)$. $\Delta\alpha$ and Δr are the angle and radial length that are used to divide the *segments* and *circles*, respectively. P_m denotes the set of points in *segment* m. P_m^n denotes the points in bin_n^m, where m and n represent the sequence numbers of *segment* and *circle*, respectively.

$$P_m = \{p_i | seg(p_i) = m\} \tag{3}$$

$$P_m^n = \{p_i | seg(p_i) = m, cir(p_i) = n\} \tag{4}$$

In each *bin*, the points with the lowest height z_i constitute

a set PL in the whole plane.

$$PL = \{p_i | p_i \in P_n^m, z_i = \min(\{z_n^m\}), \\ n = 1, 2, \ldots, N, m = 1, 2, \ldots, M\} \quad (5)$$

The lowest points in *segment* m constitutes the set SL_m.

$$SL_m = \{p_i | p_i \in PL \cap p_i \in P_m\} \quad (6)$$

However, not all the points in PL are ground points since some of them could be from vehicles, trees, buildings or false measures. The most likely points are selected as initial seeds by RLWR as described in section II.C. In this paper, the seeds means a skeleton of the ground, based on which the surface of the whole ground can be modelled.

B. GAUSSIAN PROCESS REGRESSION

1) PREDICTION

Regression is a supervised learning method, which can be used in prediction of continuous quantities. In general, the input vector is denoted as x and the output is denoted as y. The dataset D of N_D observations is denoted as $D = \{(x_i, y_i) | i = 1, \ldots, N_D\}$. The goal of regression is to move from the finite training data D to a function f that makes predictions for all possible input values [21].

A Gaussian process provides a powerful basis for modelling spatially correlated and possibly uncertain data [3]. The mean function $m(x)$ and covariance function $k(x, x')$ will completely specify a Gaussian process as

$$f(x) \sim N(m(x), k(x, x')) \quad (7)$$
$$m(x) = \mathbb{E}[f(x)] \quad (8)$$
$$k(x, x') = \mathbb{E}[(f(x) - m(x))(f(x') - m(x'))] \quad (9)$$

where x and x' are the independent variables, $f(x)$ is the function value at location x, and $\mathbb{E}$ represents mathematical expectations. For national simplicity, the mean function $m(x)$ is usually set to zero [21]. The covariance function specifies the relationship between pairs of random variables. The commonly used covariance function is the squared exponential function [3].

$$k(x_i, x_j) = \sigma_f^2 \cdot \exp(-\frac{(x_i - x_j)^2}{2l^2}) + \sigma_n^2 \delta_{ij} \quad (10)$$

where l is called length-scale, σ_f^2 is the signal variance, and σ_n^2 is the noise variance. These three parameters form the hyperparameters set $\theta = (l, \sigma_f^2, \sigma_n^2)$. δ_{ij} is a Kronecker delta, which is one if and only if $i = j$ and zero otherwise.

The joint distribution of the outputs of the training samples, $f = \{f(x_i)\}, i = 1, 2, \ldots, N_D$, and the test outputs f_* at location x_* can be defined as

$$\begin{bmatrix} f \\ f_* \end{bmatrix} \sim N\left(0, \begin{bmatrix} K(X, X) & K(X, x_*) \\ K(x_*, X) & K(x_*, x_*) \end{bmatrix}\right) \quad (11)$$

where $X = \{x_i | i = 1, 2, \ldots, N_D\}$ is the set of training inputs, and x_* is the test input. $K(X, X)$ is the covariance matrix, $K(X, X) = \{k(x_i, x_j)\}_{1 \le i,j \le N_D} \in \mathbb{R}^{N_D \times N_D}$, and similarly for the $K(X, x_*)$, $K(x_*, x_*)$ and $K(x_*, X)$. The prediction equations for GPR at location x_* are as follows [21].

$$\bar{f}_* = K(x_*, X)K(X, X)^{-1} f \quad (12)$$
$$\mathbb{V}[f_*] = K(x_*, x_*) - K(x_*, X)K(X, X)^{-1}K(X, x_*) \quad (13)$$

where $\bar{f}_*$ and $\mathbb{V}[f_*]$ are the mean and covariance of f_*, respectively. $\bar{f}_*$ is regarded as the prediction value at location x_*. $\mathbb{V}[f_*]$ denotes the accuracy of the prediction.

As described in section III, the azimuth α is utilized as independent variable and point height z is regarded as the function value at location α. The point height at location α_x can be predicted with N_α initial seeds $\{(\alpha_i, z_i) | i = 1, \ldots, N_\alpha\}$ in the same *circle* and equation (12).

2) LEARNING HYPERPARAMETERS

Before making a prediction, the hyperparameters in equation (10) should be determined first, which is called learning hyperparameters.

It is assumed that $\{(X^q, Y^q)\}_{q=1}^Q$ is a set of training data that contains Q groups of training samples, each training sample is of the form (X^q, Y^q), where $X^q = \{x_1^q, x_2^q, \ldots, x_{n_q}^q\}$ is a set of independent variables of the *qth* group, which has n_q elements. The elements in $Y^q = \{y_1^q, y_2^q, \ldots, y_{n_q}^q\}$ are the corresponding dependent variables. It is assumed that the groups are conditionally independent. Since the distribution of y is $y \sim N(0, K_q)$, the logarithm marginal likelihood of y is shown in (14). The hyperparameters can be obtained by maximizing the logarithm marginal likelihood [21].

$$\sum_{q=1}^{Q} \log p(Y^q | X^q, \theta) = -\frac{1}{2}\sum_{q=1}^{Q} (Y^q)^T K_q^{-1} Y^q \\ - \frac{1}{2}\sum_{q=1}^{Q} \log |K_q| \\ - \frac{\log 2\pi}{2}\sum_{q=1}^{Q} n_q \quad (14)$$

where K_q is the covariance matrix of noisy Y^q, and can be calculated using (10). In order to maximize the marginal likelihood in (14) and obtain the hyperparameters, the partial derivatives of the marginal likelihood are shown as follows.

$$\frac{\partial}{\partial \theta}\sum_{q=1}^{Q} \log p(Y^q | X^q, \theta) \\ = \frac{1}{2}\sum_{q=1}^{Q} tr\left(\left(a^q (a^q)^T - K_q^{-1}\right)\frac{\partial K_q}{\partial \theta}\right) \quad \text{where} a^q = K_q^{-1} Y^q \quad (15)$$

where $tr(\cdot)$ denotes the trace of the matrix. $\frac{\partial K_q}{\partial \theta}$ is a matrix of elementwise derivatives. The partial derivatives of the covariance matrix are shown below.

$$\frac{\partial K_q(x_i, x_j)}{\partial l} = \sigma_f^2 \exp(-\frac{(x_i - x_j)^2}{2l^2}) \cdot \frac{(x_i - x_j)^2}{l^3}$$

$$\frac{\partial K_q(x_i, x_j)}{\partial \sigma_f} = 2\sigma_f \exp(-\frac{(x_i - x_j)^2}{2l^2})$$
$$\frac{\partial K_q(x_i, x_j)}{\partial \sigma_n} = 2\sigma_n \delta_{ij} \tag{16}$$

Then, the gradient based optimizer is advantageous to seek the hyperparameters [22].

C. ROBUST LOCALLY WEIGHTED REGRESSION

Cleveland [23] proposed the RLWR algorithm to smooth the scatterplot and enhance the visual information, which can fit the undulating ground with the idea of piecewise fitting. RLWR can reduce the impact of outliers on the fitting. The relationship of dependent and independent variables are assumed to be modelled as

$$y_i = g(x_i) + \varepsilon_i \tag{17}$$

where x_i and $y_i (i = 1, 2, \ldots, n)$ are independent and dependent variables, respectively, and ε_i are independent and normally distributed random variables. The estimated parameters of $g(\cdot)$ are obtained by minimizing the sum of error squares

$$\sum_{i=1}^{n} B(\frac{\varepsilon_i}{6s})\omega(x_i)\varepsilon_i^2 \tag{18}$$

where $\varepsilon_i = y_i - g(x_i)$ are the residuals from the current fitted values, and s is the median of $|\varepsilon_i|$. The bisquare weight function $B(x)$ and "tricube" weight function $\omega(x)$ are defined as follows [8].

$$B(x) = \begin{cases} (1 - x^2)^2 & for\ |x| < 1 \\ 0 & for\ |x| \geq 1 \end{cases} \tag{19}$$

$$\omega(x_i) = \begin{cases} (1 - (\frac{d(x_i, x_j)}{\max_{j \in N(x_i)} d(x_i, x_j)})^3)^3 & j \in N(x_i) \\ 0 & j \notin N(x_i) \end{cases} \tag{20}$$

where $d(x_i, x_j)$ represents the distance between x_i and x_j along x direction, and $N(x_i)$ denotes the local neighborhood of x_i. There are k observations that are closet to x_i along x-space in $N(x_i)$. In this paper, the radial distance r and height z of the point clouds are regarded as independent variable and dependent variable, respectively. More detailed description of RLWR can be found in [8].

III. GROUND SURFACE MODELLING BASED ON HYBRID REGRESSION

The undulations of ground in the real scene are complicated. Ground points filtering solely based on the heights of the point clouds can not always be reliable. GPR-based method is effective on ground surface modelling, which can predict the height of the ground anywhere based on some credible ground points. In Lidar scanning scenarios, the occlusion and sparse scanning points are inevitable. Existing GPR-based method [3] can not predict the ground height accurately in the case of occlusion, and constructing the reference points of the model with fixed range thresholds can not meet the requirement of actual environments. In this section, a filtering method based on hybrid regression is introduced in detail. The points will be labeled as ground or non-ground after filtering.

A. HYPERPARAMETERS OF GPR

Before filtering, the process of learning hyperparameters is described in this section. The set $\{(A'_n, Z'_n)\}_{n=1}^{N}$ obtained in N *circles* is applied to obtain the hyperparameters $\theta = (l, \sigma_f, \sigma_n)$. A'_n is obtained by extending $A_n = \{\alpha_1^n, \alpha_2^n, \ldots, \alpha_{N_\alpha}^n\}$, which is the set of azimuth in *circle n*.

$$\alpha_i = \text{atan2}(x_i, y_i) \tag{21}$$

Z'_n is extended by $Z_n = \{z_1^n, z_2^n, \ldots, z_{N_\alpha}^n\}$, which is the corresponding heights of A_n. In each *circle*, considering the periodicity of the azimuth, the seeds that are near 0 and 2π need to be extended. The extension process is shown in (22) and Fig. 2.

$$\begin{aligned} A_0 &= \{\alpha | \alpha \in \alpha_n \cap \alpha \in [0, T_\alpha]\} + 2\pi \\ A_{2\pi} &= \{\alpha | \alpha \in \alpha_n \cap \alpha \in [2\pi - T_\alpha, 2\pi]\} - 2\pi \\ A'_n &= A_n \cup A_0 \cup A_{2\pi} \end{aligned} \tag{22}$$

where T_α represents the extension range of azimuth. After extension, the independent variables of the training azimuth are in $[-T_\alpha, 2\pi + T_\alpha]$.

In Fig. 2, the blue points represent the original seeds in a *circle*, which belong to $[0, 2\pi)$. Due to the periodicity of the *circle*, each point is associated with the points on both sides. For the points that are near 0 and 2π, the continuity of the other side is missing. Therefore, the points near edges are extended. However, after extension, there are many repeated pairs of points in each *circle*. It is shown in (10) that the covariance function decreases sharply as the distance between two points increases. Therefore, the covariance function from the farther point in each pair is almost zero and considered to be negligible. With the learning process in section II.B, the hyperparameters that are suitable for GPR in *circle* direction are obtained.

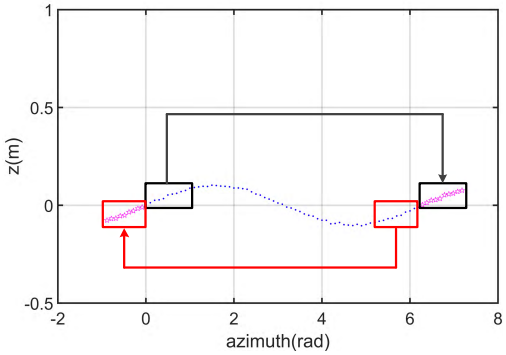

FIGURE 2. The process of azimuth extension. The blue points represent the original seeds. The magenta pentagrams are the extended points.

B. GROUND SURFACE MODELLING

The 3D point clouds processed in this paper are acquired in road environment mainly using vehicle-mounted Velodyne

Lidar HDL-64E. The ground terrains in actual scene are often complex. The abrupt changes of the ground in the case of lawns, steep slopes and railways will cause difficulties in ground filtering. In addition, when the point clouds are missing due to obstructions in some areas, the ground continuity will be broken, which will reduce the accuracy of ground prediction as well. To tackle these issues, the model that is constituted by a hybrid regression method is proposed in this section. This method consists of the following sequence of four steps.

1) Polar grid mapping. The 3D point clouds are projected onto the $x-y$ plane. The points in radius R_{pc} are divided into M *segments* and N *circles* using (1) and (2). R_{pc} denotes the range of grid map. The point clouds totally contain $M \times N$ *bins*. In each *segment* m, the lowest sampled points set SL_m is obtained with (6).
2) The RLWR filtering method in [8] is performed on SL_m in each *segment* m. After iteration, the heights of points in SL_m are replaced by the fitted ground heights to constitute set SL'_m. The aboveground outliers in SL'_m are filtered and fitted to the equivalent ground heights. The line gradient that is fitted by the neighboring points around each point in SL'_m constitutes set $grad_m$.
3) All the points in SL'_m are filtered through a gradient filter. Generally speaking, the gradient of a ground point is less than 10 degrees. The points whose gradients are more than 10 degrees are replaced with the nearest point whose gradient is less than 10 degrees. It is worth noting that the points with large gradients are obtained because of a small local neighborhood parameter k. Large k will remove more aboveground outliers, but at the expense of losing local structural information of the ground. Since the actual ground environment often includes a variety of topographic structures, a small k parameter combined with the gradient filter is used to construct the seed skeleton structure.
4) Based on the seed skeleton, GPR in circumference is applied to model the ground surface with the seeds in each *circle*. The seeds in the edges 0 and 2π are extended by the aforementioned method. For each *bin* in *circle* n, it is assumed that the maximum azimuth and the minimum azimuth that a *bin* overlaps are α_{max} and α_{min}, respectively. $\bar{\alpha} = (\alpha_{\max} + \alpha_{\min})/2$ is taken as the input of the model. The predictive height is regarded as the mean height of the *bin*. The height of each point in *bin* P_m^n is compared with the predictive height. If the height difference is less than T_g, the point is filtered as ground, otherwise labeled as non-ground.

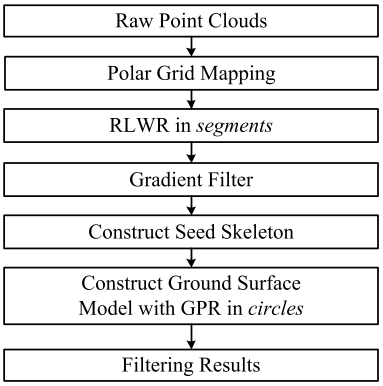

FIGURE 3. The flowchart of the hybrid regression method.

Algorithm 1 Ground Surface Filtering With a Hybrid Regression Method

Input: $P = (p_1, p_2, \ldots, p_{N_p})^T$, $\Delta\alpha$, Δr, R_{pc}, k, $\theta = (l, \sigma_f, \sigma_n)$, T_g
Output: Label of each point

$M = \left\lceil \frac{2\pi}{\Delta\alpha} \right\rceil$, $N = \left\lceil \frac{R_{pc}}{\Delta r} \right\rceil$;
$(SL_m, P_m^n) = \text{PolarGridMap}(P, M, N)$;
$seed = \emptyset$;
for $m = 1 : M$ **do**
  $(SL'_m, grad_m) = \text{RLWR}(SL_m, k)$;
  $sd_m = \text{GradientFilter}(SL'_m, grad_m)$;
  $seed = seed \cup sd_m$;
end
for n = *1:N* **do**
  $sd_n = \text{CircleSeed}(seed, n)$;
  $sd_n = \text{AzimuthExtend}(sd_n)$;
  for m = *1:M* **do**
    $\hat{z}_m^n = \text{GPR}(sd_n, P_m^n, \theta)$;
    $pointlabel = \text{HeightFilter}(\hat{z}_m^n, P_m^n, T_g)$;
  end
end

The flowchart of the hybrid regression method is shown in Fig. 3, and the filtering process is shown in Algorithm 1. The inputs include the original point clouds set P, the angular resolution $\Delta\alpha$, the distance resolution Δr, the range of grid map R_{pc}, the local neighborhood parameter for RLWR process k, the set of hyperparameters θ, and the filtering threshold T_g. After the hybrid regression analysis, each point in P is labelled as ground or non-ground.

C. COMPARISON WITH EXISTING REGRESSION-BASED METHODS

The proposed hybrid regression method has the ability to eliminate the outliers and can robustly construct the ground surface model. The RLWR process and the GPR process are complementary in ground modeling. RLWR filtering can provide more robust initial seeds to construct the seed skeleton for GPR, while the GPR process can reduce the dependence of filtering on parameters. Therefore, the combination of RLWR process and GPR process makes the ground filtering more robust in the face of complex terrain. Compared with the state-of-the-art regression-based methods in [3] and [8],

the distinctions are listed as follows.

- Unlike the GPR-based method in [3] that seeks the initial seeds with fixed height and fixed radius, the proposed method can provide a robust seed skeleton structure with RLWR process, which is more robust when filtering undulate ground.
- The filtering method with RLWR in [8] uses common filtering results in $x-z$ and $y-z$ profiles as the ground points. However, the proposed method is more suitable for filtering of point clouds received from mobile Lidar. The processing in radial and circumferential direction are more consistent with the distribution of point clouds.
- The hybrid regression method combines the advantages of RLWR-based method and GPR-based method. In radial direction, RLWR is utilized to winnow out the aboveground points and construct the seed skeleton. In circumferential direction, GPR is used to predict the ground model, which reduces the dependence on parameters of the method. In this way, the continuity of the whole plane is utilized to construct the ground model.
- When the point clouds are sparse, the GPR-based method construct the sparse seeds skeleton so that the uncertainty of the prediction becomes large. RLWR filtering is sensitive to the choice of local neighborhood parameter in different point clouds density. For the hybrid regression method, small local neighborhood parameter combined with gradient filter makes the radial filtering insensitive to point clouds density. Meanwhile, when the Lidar scanning lines are reduced, its tangential sparsity is much smaller than its radial sparsity. Therefore, the circumferential GPR process with adequate seed skeleton is usually less affected by the point clouds density.

IV. RESULTS AND DISCUSSION

In this paper, the point clouds within a radius $R_{pc} = 50m$ from the Lidar is in the spotlight. The angle $\Delta\alpha$ that is applied to divide the *segments* is set to 2 degrees. Taking into account the characteristics of point clouds received by the vehicle-mounted Lidar, the area with radius in $[0, 20]\,(m)$ is divided by radial length $\Delta r = 0.2m$ and the area with radius in $[20, 50](m)$ is divided by $\Delta r = 0.5m$. Hence, in a scan, there are totally 180 *segments* and 160 *circles*. The angular extension T_α is empirically set to 0.3π. Other parameters are set as follows: $l = 0.1935$, $\sigma_f = 0.2415$, $\sigma_n = 0.0396$.

A. DATASET

In this study, the simulated point clouds and the measured datasets are utilized to verify the performance of the proposed method. The measured datasets include ten labelled scans dataset [24], the KITTI dataset [25] and the point clouds of Quanergy M8[1].

[1]https://www.dropbox.com/sh/3s5th10h0vosj51/AAAwxex4okJ9LirNUHBLZeYUa?dl=0

1) THE SIMULATED POINT CLOUDS

In the simulation experiments, the parameters of Velodyne HDL-64E are utilized to simulate the ground model. The height of the Lidar from the ground is $1.8m$. The vertical scanning range is $(-24.8, +2)$ degrees, in which only the negative angle scanning line can get the ground returns. The horizontal scanning point is downsampled, which are taken every 2 degrees. To simulate the undulating ground, a sinusoidal function is used to model the ground heights. The range measurement accuracy is set to $2cm$. An example of the simulated point clouds are shown in Fig. 4.

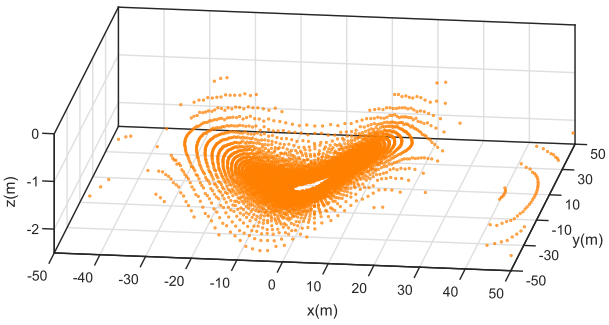

FIGURE 4. An example of the simulated point clouds. The period and amplitude of ground undulation are 50*m* and 0.5*m*, respectively.

In the experiments, the ground undulations can be simulated by changing the period and amplitude of the sinusoidal function. In Fig. 4, the missing of point clouds at [30m,40m] along x-axis is caused by the occlusion due to ground undulations.

2) TEN LABELLED SCANS DATASET

The ten labelled scans are collected by a Velodyne Lidar mounted on a moving vehicle through the urban in Boston area (Fig. 5(a)), which contains the label of each point. Fig. 6(a) shows the third scan of the dataset. There are *ground*, *car*, *fence*, *house*, *person*, *street_sign*, *tree* and *other* in the scene. In the original label, only the ground of the road and a fraction of slopes are labelled as *ground*. Some non-road ground surface is labelled as *other* (For example, the magenta points in the red rectangle.). The purpose of this paper is to segment the entire ground surface, therefore, some ground points that were once labelled as *other* are relabeled as *ground*. The other labels are integrated and relabeled as non-ground. The relabeled scan of Fig. 6(a) is shown in Fig. 6(b). All ten scans are relabeled manually to amend the mislabeled points. The ground and non-ground numbers of each scan are listed in Table. 1.

3) KITTI DATASET

The KITTI dataset is an open Lidar dataset. The dataset has been recorded from a moving platform, which was equipped with two high-resolution color and two grayscale video cameras, a Velodyne laser scanner and a combined GPS/IMU system that can provide high-precision GPS

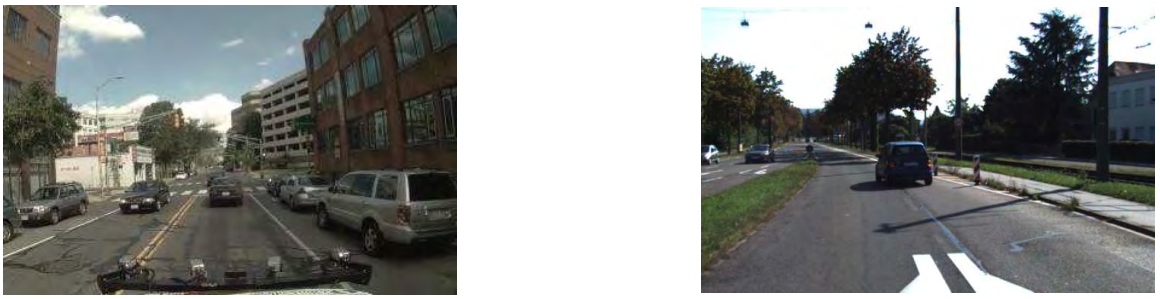

(a) (b)

FIGURE 5. The optical images of the two datasets. (a) An example of the urban scenes in Boston where the ten labelled scans were collected. (b) An example of the road scene in KITTI dataset.

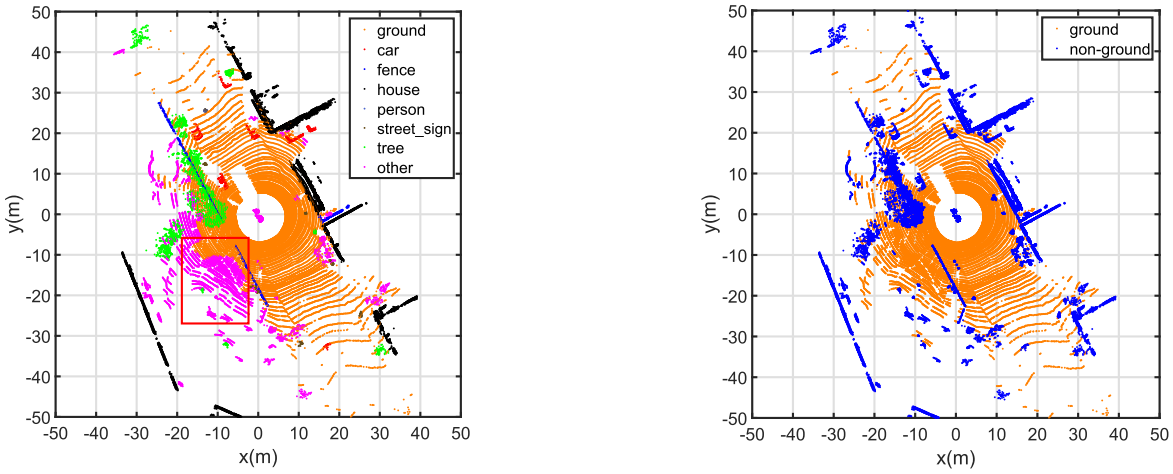

(a) (b)

FIGURE 6. Relabeled point clouds in ten labelled scans dataset. (a) Original labelled point clouds. The magenta points in red rectangle is mislabeled as *other*. (b) Relabeled point clouds. All points are divided into ground and non-ground. The ground are denoted by the orange points. The non-ground are denoted by the blue points.

TABLE 1. The relabeled ground and non-ground points of the ten labelled scans dataset.

Label	1	2	3	4	5	6	7	8	9	10	Total
ground	22060	20413	25928	19611	21545	13358	24398	22063	17792	13123	200291
non-ground	43044	44437	37022	45619	43640	52534	38405	43262	46222	53655	447840

measurements and IMU accelerations. The images of the environments are shown in Fig. 5(b). The scenes in this dataset have more complex ground terrains, such as lawns, slopes, and railways. Since the environment of this dataset is complex without supported ground truth, we have manually labelled 5 representative pieces of point clouds. The numbers of ground and non-ground points in each pieces are shown in Table. 2 and the point clouds are shown in Fig. 13–Fig. 16.

4) THE DATASETS OF QUANERGY M8

Quanergy M8 has eight scanning layers with the vertical scanning range of 20 degrees (−17 degrees to +3 degrees). The scanning frequency of the data used in the experiments is 10Hz. The Lidar is stationary on a slope and is about 0.8m above the ground. Taking into account the height of Lidar, the ground filtering ranges are set to 30m. The first ten scans of point clouds are labelled manually for experiments. The ground and non-ground numbers of each scan are listed in Table. 3. Fig. 7 shows an example of 3D point clouds of M8.

TABLE 2. The manually labelled 5 pieces of point clouds in KITTI dataset.

Label	Piece1	Piece2	Piece3	Piece4	Piece5
ground	3040	470	12248	4682	2669
non-ground	4769	42	10126	4350	792

TABLE 3. The manually labelled ground and non-ground points of Quanergy M8.

Label	1	2	3	4	5	6	7	8	9	10	Total
ground	11944	11722	11741	11775	11805	11747	11717	11824	11920	11777	117972
non-ground	7448	7618	7560	7560	7582	7601	7643	7558	7444	7637	75651

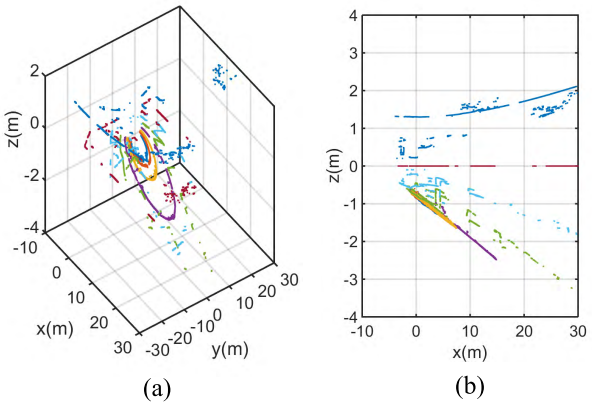

FIGURE 7. The 3D point clouds obtained from M8. Different colors denote different scanning lines of the Lidar. (a) 3D view. (b) Side view.

B. COMPARISON METHODS INTRODUCTIONS

The comparison methods in this paper includes the histogram-based method in [26], the GPR-based method in [3] and the RLWR-based method in [8]. In this section, the conditions and the filtering processes of the three methods are described.

In histogram-based method, the histogram statistics are performed on the heights of point clouds. The width of bins in the histogram is set to $0.2m$. If there is only one peak in the histogram, the position of the peak is regarded as the height of ground h. The points whose heights are less than $h+T_g$ are filtered out as ground points. T_g is a predefined threshold and is set to $0.3m$. If there are multiple peaks in the histogram, the peak at the lowest position is considered to be the height of ground.

The process of the GPR-based method is the same as in [3]. Since the ground complexity of the two datasets is different, the filtering thresholds T_g are set to $0.15m$ and $0.3m$ for ten labelled dataset and KITTI dataset, respectively.

The RLWR-based method used in this paper is slightly different from the original method in [8]. As shown in [8], it takes 336.51s to filter the point clouds with 32822 points. Since the number of points in each frame in KITTI is more than one hundred thousand, filtering the ground points by original RLWR will take a long time. In this paper, the RLWR is implemented on the lowest points of the *bins* in each *segment*. The fitting height h is taken as the average height of the bin and all the points in that bin is filtered with $h + T_g$. T_g is the predefined threshold that is set to $0.2m$ and $0.4m$ for ten labelled dataset and KITTI dataset, respectively.

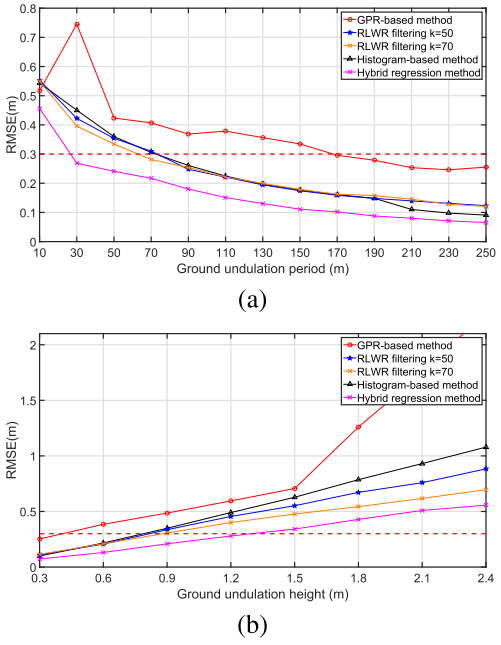

FIGURE 8. The Root Mean Square Error results of four methods. (a) and (b) show the variation of RMSE values with the period and height, respectively. The red dashed line indicates a threshold of $0.3m$.

C. GROUND MODELING OF SIMULATED POINT CLOUDS

In the simulation experiments, the Root Mean Square Error (RMSE) is utilized to measure the modelling accuracy of different methods.

$$RMSE = \sqrt{\frac{1}{N_z}\sum_{n=1}^{N_z}(\hat{z}_n - z_n)^2} \tag{23}$$

where $\hat{z}_n$ and z_n represent the height prediction and ground truth of point n, respectively. N_z is the number of points in the point cloud.

The modeling results are shown in Figure. 8. In Figure. 8(a), the ground height is set to $0.5m$. In Figure. 8(b), the period is set to $150m$.

In Fig. 8, as the ground undulation period decreases, or the undulation amplitude increases, the RMSE of all filtering methods increases. Among these methods, the hybrid regression method performs the best at all periods and amplitudes. It is worth noting that when the period is $10m$, the RMSE of GPR-based method is smaller than the value in the period of $30m$. This is because the fixed range used by the GPR-based method to find the initial seeds is $30m$. When the period is less than $30m$, the initial seeds can be found in multiple periods. Although some ground undulation details

TABLE 4. The filtering results of the proposed method and compared methods on ten labelled scans dataset.

Method	TP	FP	FN	TN	Type I error (%)	Type II error (%)	Total error (%)	Accuracy (%)
GPR-based method	191814	8477	6633	441207	4.23	1.48	2.33	97.67
RLWR filtering	194962	5329	12380	435460	2.66	2.76	2.73	97.27
Histogram-based method	171421	28870	5646	442194	14.41	1.26	5.33	94.67
Hybrid regression method	194251	6040	5727	442113	3.02	1.28	1.82	**98.18**

are missing, more ground seeds will be obtained. Therefore, the points that are predicted accurately become more and the RMSE value becomes smaller than RMSE in period $= 30m$.

As a result, if RMSE $= 0.3m$ (the red dashed line in Fig. 8) is set as a threshold to judge whether the modeling is accurate or not, under the experimental conditions, the hybrid regression filtering performs well in the case where the ground undulation period is larger than $30m$ and the height difference is less than $2.4m$, which shows that the proposed method can filter most common undulating ground in real scenes in theory.

D. GROUND SURFACE FILTERING ON THE FLAT URBAN SCENES

In this section, ten labelled scans dataset are utilized to validate the performance of the hybrid regression method. k is set to 20 in RLWR stage and T_g is set to 0.2m. The evaluation indexes in [8] and [27] are employed in comparison, which consists Type I and Type II errors, total error and accuracy.

$$\text{TypeIerror} = \frac{FP}{TP + FP} \tag{24}$$

$$\text{TypeIIerror} = \frac{FN}{FN + TN} \tag{25}$$

$$\text{Totalerror} = \frac{FP + FN}{TP + FP + FN + TN} \tag{26}$$

$$\text{Accuracy} = \frac{TP + TN}{TP + FP + TN + FN} \tag{27}$$

where TP is the number of ground points that are segmented correctly. TN is the number of non-ground points that are segmented correctly. FP is the number of ground points that are segmented as non-ground. FN is the number of non-ground points that are segmented as ground.

The comparative results are shown in Table. 4. The filtering accuracy by the proposed method reaches 98.18%, which is 0.51% higher than GPR-based method, 3.51% higher than the histogram-based method, and 0.91% higher than the RLWR filtering. The ground truth and filtering results of the 5th frame in ten labelled dataset are shown in Fig. 9, Fig. 10 and Fig. 11, respectively. As shown in Fig. 9, the ground in red rectangle (Marked 3) is a slope. Since GPR-based method uses fixed height threshold to find the initial seeds and model the ground surface, it is difficult to construct a complete ground seeds with a slope that rapidly falls outside the threshold. The inaccurate model reduce the efficiency of filtering, which is shown in Fig. 10(a). The filtering of the histogram method in Fig. 10(b) is also affected by the slope. Slowly changed ground height does not affect the peak position of the histogram but increase the range of the height. The fixed height threshold can not satisfy the requirement of undulating ground filtering. In the case of sloped ground, the hybrid regression method and RLWR filtering perform well, which are shown in Fig. 10(c) and Fig. 11(a)(d).

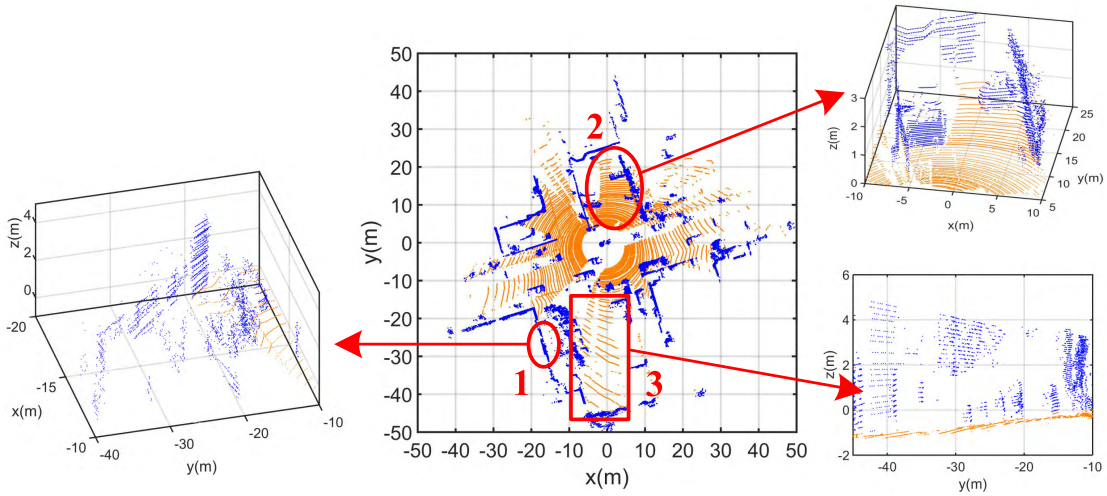

FIGURE 9. The ground truth of the 5th frame in ten labelled dataset. The details of partial enlargement of piece 1, 2, and 3 are shown in 3D view. The orange points indicate the ground, and the blue points indicate the aboveground objects.

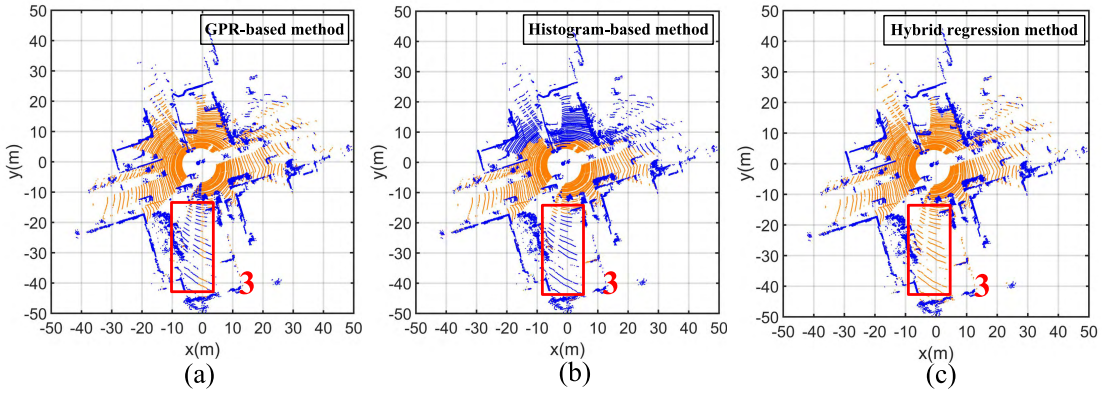

FIGURE 10. The filtering results of the 5th frame in ten labelled dataset. (a), (b), and (c) are the filtering results of GPR-based method, histogram-based method and hybrid regression method, respectively. The orange points indicate the ground, and the blue points indicate the aboveground objects.

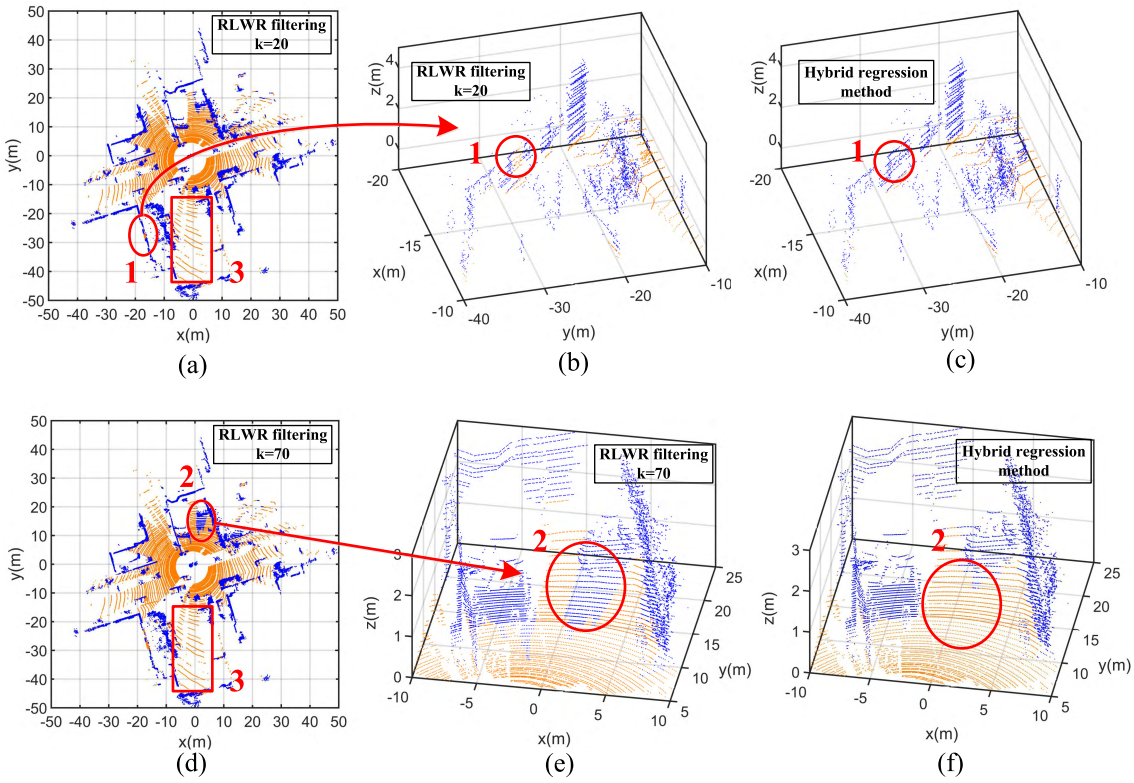

FIGURE 11. The filtering results of the 5th frame in ten labelled dataset. (a) RLWR filtering result with $k = 20$. (b) Detail of partial enlargement of Piece 1 of (a). (c) Filtering result of piece 1 with hybrid regression method. (d) RLWR filtering result with $k = 70$. (e) Detail of partial enlargement of piece 2 of (d). (f) Filtering result of piece 2 with hybrid regression method. The orange points indicate the ground, and the blue points indicate the aboveground objects.

Fig. 11(a) and (d) show the filtering results of RLWR method with $k = 20$ and $k = 70$, respectively. As shown in (a) and (d), most ground points are filtered correctly. However, no matter whether k takes a large value or a small value, there are some cases where the ground points cannot be accurately filtered out. In general, small local neighborhood parameter k is helpful to fit the local change of the ground. But some vertical walls and trees will be mistakenly filtered to the ground. The partial enlargement of the red circle area (Piece 1) of Fig. 11(a) is shown in Fig. 11(b). Large k can smooth the ground, but it reduces the local changes of the ground height and will easily get erroneous filtering. The partial enlargement of the red circle area (Piece 2) in Fig. 11(d) is shown in Fig. 11(e). The ground point clouds that are near the vehicle are mislabelled. The proposed hybrid regression method uses the gradient filter and GPR process to solve

FIGURE 12. The optical images of the four scenes. (a) The image of 0057 dataset. (b) and (c) are the images of 0056 dataset. (d) The image of 0051 dataset.

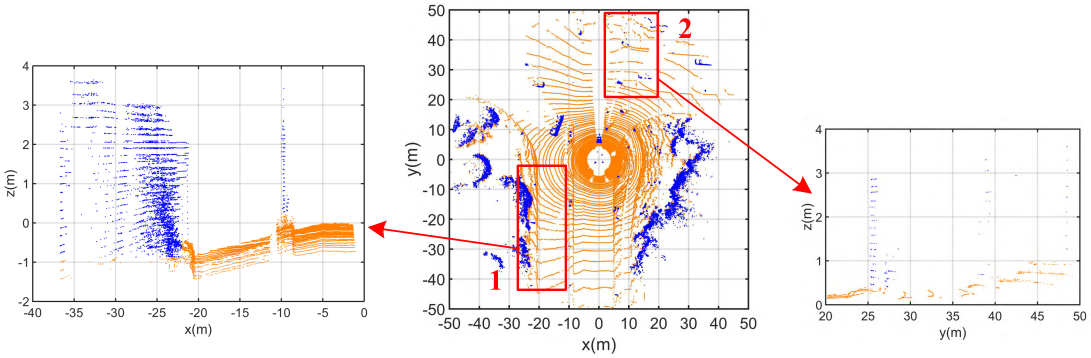

FIGURE 13. The ground truth of point clouds in 0057 dataset. The details of partial enlargement of piece 1 and 2 are shown in 3D view. The orange points indicate the ground, and the blue points indicate the aboveground objects.

the problem of parameter selection. The details of partial enlargement of hybrid regression filtering at the same areas as (b) and (e) are shown in (c) and (f), respectively, which shows better performance than RLWR filtering.

E. GROUND SURFACE MODELLING ON THE COMPLEX ROAD SCENES

Some frames of point clouds in 2011_09_26_drive_0051, 2011_09_26_drive_0056 and 2011_09_26_drive_0057 datasets from KITTI website are utilized to validate the performance of the filtering methods. The grounds in these three datasets are more complex compared with the ten labelled scans dataset. As shown in Fig. 12, the ground has various morphologies, including roads, railways, lawns and so on. In order to fit the complex ground better, the local parameter k is set to 10 in this section, and the threshold T_g is set to $0.4m$. The filtering results of several typical scans are shown below.

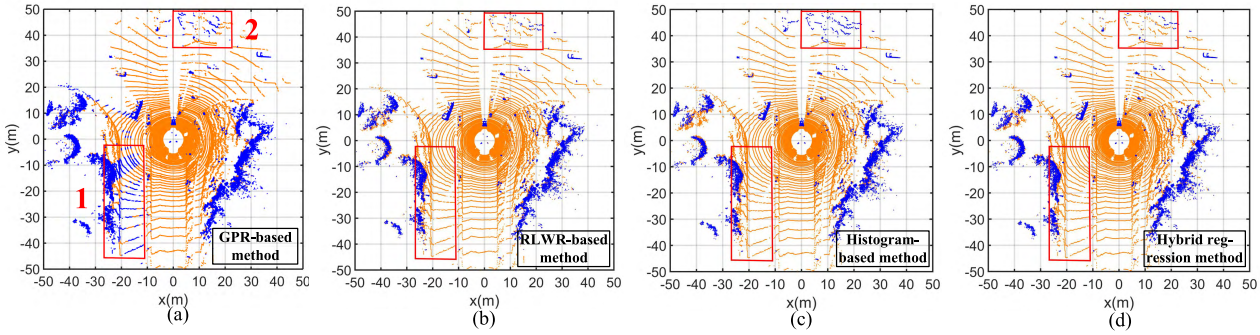

FIGURE 14. The filtering results of point clouds in 0057 dataset. The orange points indicate the ground, and the blue points indicate the aboveground objects.

In Fig. 13, two pieces in the scene represent typical undulating ground. From the partially enlarged side view of the two pieces, it can be seen that the relative height of the ground changes by more than 1m. The loss of initial seeds results in a modelling failure with GPR, as shown in Fig. 14(a). The filtering of other three methods can be regarded as identical with the result from visual inspection. More detailed statistical results are shown in Table. 5. Among the four methods, the proposed method reaches the highest accuracy of 76.81%.

Fig. 15 shows the filtering cases when the point clouds are partially missed due to occlusion. As seen in Fig. 12(b) and (c), the scene includes a variety of ground terrains such as lawn, road, and railway. The ground self-occlusion caused by height changes of different terrains results in the points missing in some areas. The filtering results from the four methods are shown in Table. 6. For the points before and after the blank area, the relevancy between the radial points is weak, which will result in a large deviation of the prediction with GPR model. RLWR-based method will smooth the ground surface near the occlusion and cannot fit the local ground undulation well. The histogram-based method focuses only on the distribution of the most ground points, not on the ground details, so the filtering results are not accurate enough. In total, in the case of occlusion, the proposed method shows good filtering performance with the accuracy of 91.38%.

TABLE 5. The filtering results of the proposed method and compared methods on piece1 and piece2.

Method	TP	FP	FN	TN	Type I error (%)	Type II error (%)	Total error (%)	Accuracy (%)
GPR-based method	1962	1548	1384	3427	44.10	28.77	35.24	64.76
RLWR Filtering	3436	74	2158	2653	2.11	44.86	26.82	73.18
Histogram-based method	3219	291	2402	2409	8.29	49.93	32.36	67.64
Hybrid regression method	3450	60	1870	2941	1.71	38.87	23.19	**76.81**

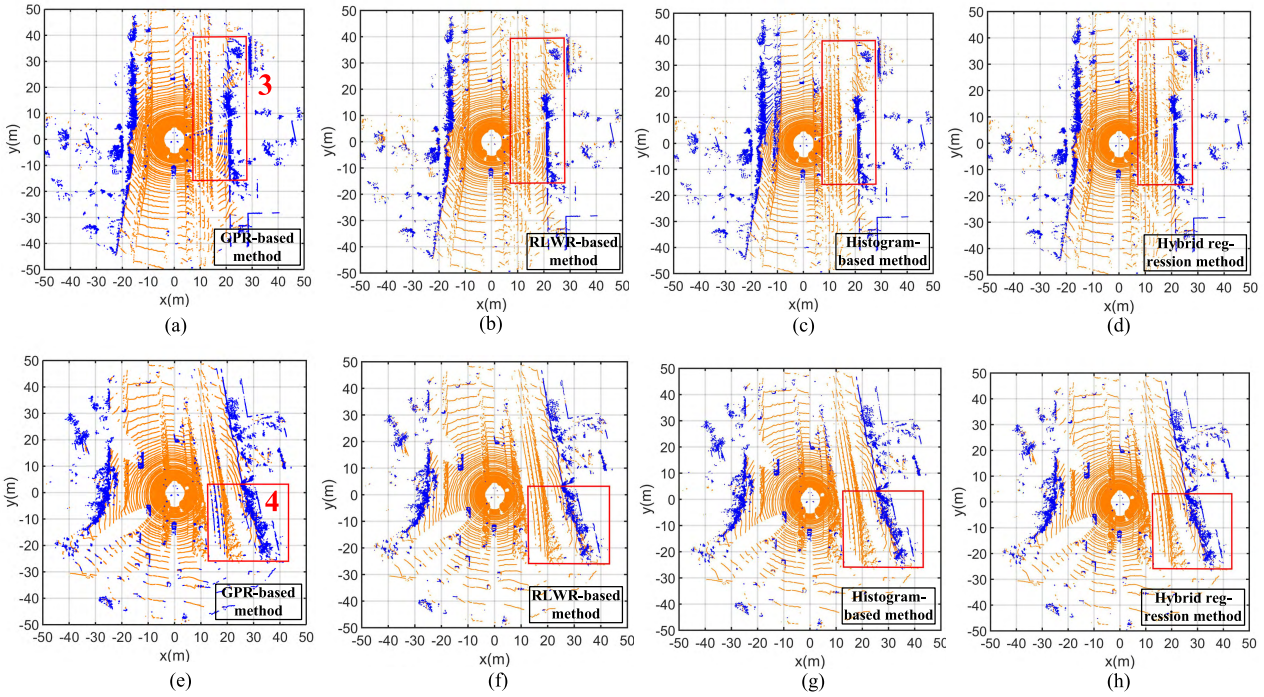

FIGURE 15. The filtering results of point clouds in 0056 dataset. (a)-(d) denote the results of scene one. (e)-(h) denote the results of scene two. The orange points indicate the ground, and the blue points indicate the aboveground objects.

TABLE 6. The filtering results of the proposed method and compared methods on piece 3 and piece 4.

Method	TP	FP	FN	TN	Type I error (%)	Type II error (%)	Total error (%)	Accuracy (%)
GPR-based method	14905	2025	2115	12361	11.96	14.61	13.18	86.82
RLWR Filtering	16928	2	4183	10293	0.01	28.90	13.33	86.67
Histogram-based method	16930	0	3597	10879	0	24.85	11.45	88.55
Hybrid regression method	16930	0	2707	11769	0	18.70	8.62	**91.38**

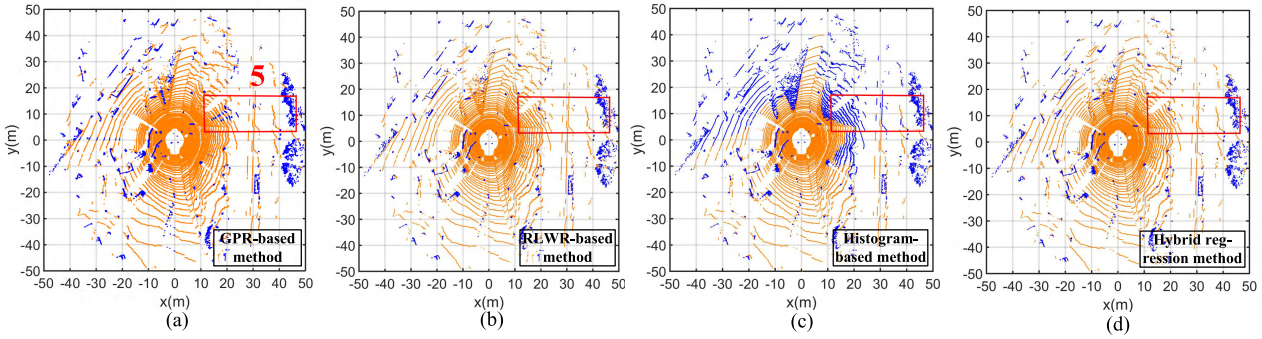

FIGURE 16. The filtering results of point clouds in 0051 dataset. The orange points indicate the ground, and the blue points indicate the aboveground objects.

TABLE 7. The filtering results of the proposed method and compared methods on piece 5.

Method	TP	FP	FN	TN	Type I error (%)	Type II error (%)	Total error (%)	Accuracy (%)
GPR-based method	2465	204	93	699	7.64	11.74	8.58	91.42
RLWR Filtering	2669	0	165	627	0	20.83	4.77	95.23
Histogram-based method	1002	1667	0	792	62.46	0	48.17	51.83
Hybrid regression method	2669	0	145	647	0	18.31	4.19	**95.81**

Fig. 16 shows the filtering results with sparse point clouds. In this scene, the histogram-based method gets poor filtering results. The histogram-based method is greatly affected by the fluctuation of the ground heights. It can only filter out the flat ground points ignoring the details of the ground. The GPR method may be affected by the increase distance in radial direction when processing sparse point clouds. RLWR and the proposed filtering obtain similar results in this case. The filtering results are displayed in Table. 7.

Broadly speaking, from the filtering results in Table. 5, 6 and 7, RLWR filtering, GPR-based filtering and the proposed method are more robust than histogram-based method in case of undulating ground, occlusion and sparse point clouds. The histogram-based method is sensitive to the height distribution of the ground. The accuracy of GPR-based method will decrease in case of sparse point clouds. The correlation between the radial points weakens and the prediction error of the model increases. RLWR filtering performs well in the case of gently changed ground. Compared with RLWR, the hybrid regression method can get higher filtering accuracy with the actual ground with multiple terrains.

F. GROUND SURFACE FILTERING OF SPARSE POINT CLOUDS

The sparse point clouds from Quanergy M8, an eight-layer lidar, are experimented in this section. Considering that the point clouds of M8 are sparse, the radial length Δr of polar grid map is set to $0.1m$ in the range of $20m$ and $0.3m$ outside the range of $20m$. Fig. 17 shows one scan of filtering results of the manually labelled data. The filtering results are shown in Table. 8.

The filtering results in Fig. 17 are consistent with the statistical results in Table. 8. Since the GPR-based method uses the height threshold to collect the initial seeds, the obtained seeds are limited when the ground is a slope, which results in predicting the ground height inaccurately. The histogram-based method is also inaccurate for modelling slopes. By comparing Table. 4 and Table. 8, it can be seen that the filtering results of RLWR-based method and the proposed hybrid regression method are both affected by the sparse point clouds. Due to the sparse point clouds, the point numbers are less in some *segments*, making it difficult to fit the ground line exactly. For example, the point clouds are sparse near the line $y = 0$ in Fig.17, so the error between the fitting line and the real

TABLE 8. The filtering results of the proposed method and compared methods on point clouds of Quanergy M8.

Method	TP	FP	FN	TN	Type I error (%)	Type II error (%)	Total error (%)	Accuracy (%)
GPR-based method	100304	17668	13752	61899	14.98	18.18	16.23	83.77
RLWR Filtering	110882	7090	21609	54042	6.01	28.56	14.82	85.18
Histogram-based method	59186	58786	6830	68821	49.83	9.03	33.89	66.11
Hybrid regression method	112422	5550	15640	60011	4.70	20.67	10.94	**89.06**

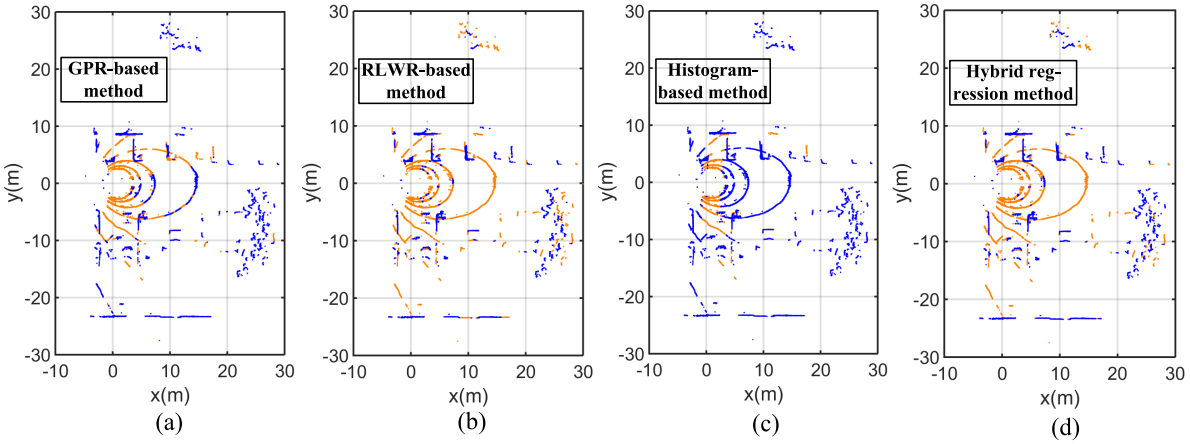

FIGURE 17. The filtering results of point clouds of Quangery M8. The orange points indicate the ground, and the blue points indicate the aboveground objects.

TABLE 9. The pros and cons of the proposed hybrid regression method.

Advantages
1. The ground with occlusions can be well predicted.
2. The ground with sparse point clouds can be well modelled.
3. The trend of ground undulation can be well fitted.
4. The filtering processes are consistent with the characteristics of on-board Lidar point clouds.
Shortcomings
1. Some details of the ground fluctuations may be smoothed.
2. Computational time. (Table. X)

TABLE 10. The computational time on a frame of the point clouds of Quanergy M8.

Method	GPR-based	RLWR	Histogram-based	Hybrid regression
Time(ms)	300	846	11	888

(**Note**: The computer is with an Intel Core i7 CPU with 4GHZ dominant frequency and 16GB main memory. The experiments are conducted in MATLAB R2014b.)

ground will be large. Therefore, in Fig. 17(b) and (d), some ground points are misclassified as non-ground points. Nevertheless, the proposed hybrid regression method still achieves 89% filtering accuracy on such undulating ground with sparse point clouds, which is the best result among the comparison methods.

G. ABOUT THE HYBRID REGRESSION METHOD

As seen in the experiments of simulated point clouds and the measured data, the proposed hybrid regression method models the ground well even in the cases of ground undulation, occlusion, and sparse point clouds. However, the proposed method also has some shortcomings. The pros and cons of the proposed method are listed as follows.

V. CONCLUSIONS

A novel ground surface modelling method based on a hybrid regression method is proposed to filter the ground of 3D point clouds in this paper. The filtering based on hybrid regression has the ability to eliminate the influence of the outliers and can robustly model the actual ground surface. This method constructs the ground seed skeleton with radial fitting and predicts the ground height in circumferential direction based on the ground seeds. In this way, the method uses the continuity of the whole plane and simplifies 2D modelling to 1D fitting. The comparative experiments with GPR-based filtering, RLWR-based filtering and histogram-based filtering show that the proposed method can perform well in most real scenarios even in the cases of ground undulation, occlusion, and sparse point clouds.

REFERENCES

[1] L. Yan, H. Liu, J. Tan, Z. Li, H. Xie, and C. Chen, "Scan line based road marking extraction from mobile LiDAR point clouds," *Sensors*, vol. 16, no. 6, p. 903, 2016.
[2] M. Giorgini, F. Barbieri, and J. Aleotti, "Ground segmentation from large-scale terrestrial laser scanner data of industrial environments," *IEEE Robot. Autom. Lett.*, vol. 2, no. 4, pp. 1948–1955, Oct. 2017.
[3] T. Chen, B. Dai, R. Wang, and D. Liu, "Gaussian-process-based real-time ground segmentation for autonomous land vehicles," *J. Intell. Robot. Syst.*, vol. 76, nos. 3–4, pp. 563–582, Dec. 2014.
[4] Y. Maalej, S. Sorour, A. Abdel-Rahim, and M. Guizani, "Vanets meet autonomous vehicles: Multimodal surrounding recognition using manifold alignment," *IEEE Access*, vol. 6, pp. 29026–29040, 2018.
[5] C. Guo, W. Sato, L. Han, S. Mita, and D. McAllester, "Graph-based 2D road representation of 3D point clouds for intelligent vehicles," in *Proc. IEEE Intell. Vehicles Symp. (IV)*, Jun. 2011, pp. 715–721.
[6] T. Chen, R. Wang, B. Dai, D. Liu, and J. Song, "Likelihood-field-model-based dynamic vehicle detection and tracking for self-driving," *IEEE Trans. Intell. Transp. Syst.*, vol. 17, no. 11, pp. 3142–3158, Nov. 2016.
[7] S. Zeng, "An object-tracking algorithm for 3-D range data using motion and surface estimation," *IEEE Trans. Intell. Transp. Syst.*, vol. 14, no. 3, pp. 1109–1118, Sep. 2013.
[8] A. Nurunnabi, G. West, and D. Belton, "Robust locally weighted regression techniques for ground surface points filtering in mobile laser scanning three dimensional point cloud data," *IEEE Trans. Geosci. Remote Sens.*, vol. 54, no. 4, pp. 2181–2193, Apr. 2016.

[9] M. Zhang, D. D. Morris, and R. Fu, "Ground segmentation based on loopy belief propagation for sparse 3D point clouds," in *Proc. Int. Conf. 3D Vis.*, Oct. 2015, pp. 615–622.
[10] K. Zhang, S.-C. Chen, D. Whitman, M.-L. Shyu, J. Yan, and C. Zhang, "A progressive morphological filter for removing nonground measurements from airborne LIDAR data," *IEEE Trans. Geosci. Remote Sens.*, vol. 41, no. 4, pp. 872–882, Apr. 2003.
[11] P. Li, H. Wang, and Z. Liu, "A morphological LiDAR point cloud filtering method based on fake scan lines," in *Proc. Int. Conf. Electron., Commun. Control (ICECC)*, Sep. 2011, pp. 1228–1231.
[12] B. Douillard *et al.*, "Hybrid elevation maps: 3D surface models for segmentation," in *Proc. IEEE/RSJ Int. Conf. Intell. Robots Syst.*, Oct. 2010, pp. 1532–1538.
[13] L.-K. Lee and S.-Y. Oh, "Fast and efficient traversable region extraction using quantized elevation map and 2D laser rangefinder," in *Proc. 47st Int. Symp. Robot. (ISR)*, Jun. 2016, pp. 1–5.
[14] B. Douillard *et al.*, "On the segmentation of 3D LIDAR point clouds," in *Proc. IEEE Int. Conf. Robot. Autom.*, May 2011, pp. 2798–2805.
[15] Y. Zhou *et al.*, "A fast and accurate segmentation method for ordered LiDAR point cloud of large-scale scenes," *IEEE Geosci. Remote Sens. Lett.*, vol. 11, no. 11, pp. 1981–1985, Nov. 2014.
[16] M. Arastounia and D. Lichti, "Automatic object extraction from electrical substation point clouds," *Remote Sens.*, vol. 7, no. 11, pp. 15605–15629, 2015.
[17] J. Byun, K.-I. Na, B.-S. Seo, and M. Roh, *Drivable Road Detection With 3D Point Clouds Based on the MRF for Intelligent Vehicle*, vol. 105, no. 2. Berlin, Germany: Springer, 2015, pp. 49–60.
[18] W. L. Lu, K. P. Murphy, J. J. Little, A. Sheffer, and H. Fu, "A hybrid conditional random field for estimating the underlying ground surface from airborne LiDAR data," *IEEE Trans. Geosci. Remote Sens.*, vol. 47, no. 8, pp. 2913–2922, Aug. 2009.
[19] M. Himmelsbach, F. V. Hundelshausen, and H.-J. Wuensche, "Fast segmentation of 3D point clouds for ground vehicles," in *Proc. IEEE Intell. Vehicles Symp. (IV)*, Jun. 2010, pp. 560–565.
[20] T. Lang, C. Plagemann, and W. Burgard, "Adaptive non-stationary kernel regression for terrain modeling," in *Proc. Robot., Sci. Syst.*, Jun. 2007, pp. 81–88. doi: 10.15607/RSS.2007.III.011.
[21] C. E. Rasmussen, C. K. I. Williams, and F. Bach, *Gaussian Processes for Machine Learning*. Cambridge, MA, USA: MIT Press, 2006.
[22] S. O. H. Madgwick, A. J. L. Harrison, and R. Vaidyanathan, "Estimation of IMU and MARG orientation using a gradient descent algorithm," in *Proc. IEEE Int. Conf. Rehabil. Robot.*, Jun. 2011, pp. 1–7.
[23] W. S. Cleveland, "Robust locally weighted regression and smoothing scatterplots," *J. Amer. Stat. Assoc.*, vol. 79, no. 368, pp. 829–836, 1979.
[24] K. Lai and D. Fox, "Object recognition in 3D point clouds using Web data and domain adaptation," *Int. J. Robot. Res.*, vol. 29, no. 8, pp. 1019–1037, 2010.
[25] A. Geiger, P. Lenz, C. Stiller, and R. Urtasun, "Vision meets robotics: The KITTI dataset," *Int. J. Robot. Res.*, vol. 32, no. 11, pp. 1231–1237, Sep. 2013.
[26] M. T. Vaaja *et al.*, "Luminance-corrected 3d point clouds for road and street environments," *Remote Sens.*, vol. 7, no. 9, pp. 11389–11402, 2015.
[27] G. Sithole and G. Vosselman, "Experimental comparison of filter algorithms for bare-earth extraction from airborne laser scanning point clouds," *J. Photogramm. Remote Sens.*, vol. 59, nos. 1–2, pp. 85–101, 2004.

KAIQI LIU received the B.S. degree from the School of Electronic and Information Engineering, Beihang University, Beijing, China, in 2013, where she is currently pursuing the Ph.D. degree with the School of Electronic and Information Engineering. Her research interests include 3D point clouds processing, point clouds segmentation, and Lidar-based objects detection.

WENGUANG WANG received the B.S. degree from Jianghan Petrolum University, Jingzhou, China, in 1997, and the Ph.D. degree from Beihang University, Beijing, China, in 2007, where he is currently an Associate Professor with the School of Electronic and Information Engineering. His research interests include signal processing, target detection and tracking, and image understanding.

RATNASINGHAM THARMARASA received the B.Sc.Eng. degree in electronic and telecommunication engineering from the University of Moratuwa, Moratuwa, Sri Lanka, in 2001, and the M.A.Sc. and Ph.D. degrees in electrical engineering from McMaster University, Hamilton, ON, Canada, in 2003 and 2007, respectively.

From 2001 to 2002, he was an Instructor in electronic and telecommunication engineering with the University of Moratuwa. From 2002 to 2007, he was a Graduate Student/Research Assistant with the Department of Electrical and Computer Engineering, McMaster University, where he is currently a Research Associate. His research interests include target tracking, information fusion, and sensor resource management.

JUN WANG received the B.S. degree from Northwestern Polytechnic University, Xi'an, China, in 1995, and the M.S. and Ph.D. degrees from Beihang University, Beijing, China, in 1998 and 2001, respectively, where he is currently a Full Professor with the School of Electronic and Information Engineering. His research interests include signal processing, DSP/FPGA real-time architecture, and target recognition and tracking.

YAN ZUO received the B.S. degree in control theory and application from North China Electric Power University, in 2003, and the Ph.D. degree in control science and engineering from Shanghai Jiao Tong University, in 2007. From 2016 to 2017, she was a Visiting Professor with the School Electrical Computer Engineering, McMaster University, Canada. She is currently an Associate Professor with the School of Automation, Hangzhou Dianzi University. Her research interests include sensor resource management, target tracking, and passive localization algorithm.